Catalytic Activity and Kinetic Studies of Core@Shell Nanostructure NiFe$_2$O$_4$@TiO$_2$ for Photocatalytic Degradation of Methyl Orange Dye

Mutawara Mahmood Baig, Erum Pervaiz, Muhammad Junaid Afzal
[1]Department of Chemical Engineering, School of Chemical & Materials Engineering (SCME),
National University of Sciences & Technology (NUST), Islamabad, Pakistan
erum.prevaiz@scme.nust.edu.pk*

Summary: Current research focuses on synthesis and characterization of magnetically separable core@shell (NiFe$_2$O$_4$@TiO$_2$) nanostructured photocatalyst with different weight percent (10, 20, 30, and 40) TiO$_2$ using simple wet chemical techniques. Magnetic core with TiO$_2$ shell was synthesized by the hydrolysis of TTIP precursor with NiFe$_2$O$_4$ nanoparticles. NiFe$_2$O$_4$ nanoparticles were synthesized by the sol-gel auto combustion method. The synthesized nanostructures were characterized for structural, morphological and magnetic behavior using XRD, TEM, SEM and VSM while the surface area was calculated using Brunauer-Emmett-Teller analyzer. Pure nickel ferrite was indexed as spinel FCC crystal structure while anatase titania was confirmed from the characteristic peaks in the indexed XRD patterns. SEM images show the uniform particle size and spherical morphology with average size of 18.85 nm±2nm. The Surface area of prepared core@shell nanostructures was found as 258 m^2/g for 10 wt. % TiO$_2$ photocatalyst. A decrease in surface area has been observed with the increase in TiO$_2$ percentage. The photo-catalytic degradation of MO was studied using UV-Visible spectroscopy under NiFe$_2$O$_4$-TiO$_2$ catalyst. UV-spectra revealed degradation of methyl orange by the decrease in the characteristic peak at 460 nm. Kinetics of degradation reaction were studied by the integral method of analysis using UV absorbance data at 460 nm. The photo-catalytic activity of as synthesized catalyst was enhanced many folds as compared to the pure nickel ferrite. M-H curves obtained from VSM revealed a decrease in the magnetization of nickel ferrite with a coating of non-magnetic TiO$_2$.

Keywords: Photocatalysis, Magnetic nanoparticles, Core-shell nanostructures, Spinel ferrites, Titania.

Introduction

Textile industry shares a significant part in water pollution by adding a variety of organic and inorganic dyes in wastewater that needs to be treated before its mixing with fresh water streams. Increasing pollution problems emerged a need to find a solution that is cost effective, recyclable and reliable. As this is the era of nanomaterials, so research is being carried out worldwide to fabricate materials that can help in the efficient removal of pollutants from the environment as well as wastewater. Due to the large surface area and diverse properties, nanomaterials are tunable for many applications, including electronics, biomaterials, energy, and environment [1-3]. Spinel ferrites (AB$_2$O$_4$) are one of the ceramic oxides, which exhibit huge compositional diversity, chemical and thermal stability and hybrid electrical & magnetic character at the same time [4]. Thus, the inert behavior of spinel ferrite has increased its usage as a catalytic material. In the past few decades, solar energy such as photocatalysis has been used as a wider solution for water-based organic dyes. The photocatalytic technology has been demonstrated to be effective for waste and drinking water treatment, water disinfection, photoreduction of carbon dioxide or nitrogen and many other applications [5]. Advance oxidation processes (AOPs), rely on the generation of highly reactive and oxidizing hydroxyl radical (•OH), are promising techniques for water treatment processes because of their exemplary performance on toxin reduction, low cost and photochemical stability [6]. Metal oxide nanostructures are widely employed in numerous applications [7-12] including AOPs because of their remarkable physicochemical properties [13]. A number of oxides, noble metals, and composites of oxides have been employed as photocatalysts. However, effective photocatalysis with good percent degradation of dye and activity remains a challenge. Therefore, a need is there to use the materials in combination to exploit their properties. Core@shell nanostructures have drawn numerous interest these days because of their fascinating uses in the field of magnetism, electronics, and catalysis. Unlike single-component catalysts, core@shell nanostructures are designed to integrate multiple properties into a single system. Furthermore, composites having a core of magnetic material are conveniently extracted in a magnetic field.

Among numerous AOPs, titania is the most commonly used catalyst in heterogeneous photocatalysis, due to its photostability, nontoxicity, competitive cost, and is stable in water under severe

---

*To whom all correspondence should be addressed.

environmental circumstances. It is also an excellent inorganic semiconductor and has environmental as well as temperature stable dielectric properties [4]. A number of research papers regarding applications of the magnetic nanomaterials containing titanium dioxide have been reported [14-31]. Nevertheless, until now, maximum research has concentrated on the titania based nanoparticles for photocatalysis applications [14-22]. Since titania is an electrical insulator, the major problem with its use in the applications mentioned above, is its extraction from treated water. However, by using the special methods, we can synthesize core@shell nanoparticles comprising a core of magnetic material and a shell of photocatalytic material and the problem of catalyst recovery can be solved by using the small magnetic field.

Hence, synthesis of titania photocatalyst having a core of magnetic material has provided a route of resolving the problems linked with the extraction of titania photocatalyst from the treated water. However, it is not easy to synthesize core@shell nanostructure of titania particles with ultraviolet light photo-activity without losing the magnetic features. Nowadays, transition elements such as nickel, cobalt, iron and strontium are used as core materials. As these metals are more stable, they show excellent results in the degradation of organic compounds. Kim et al. [32] synthesized $NiFe_2O_4$ - TiO_2 nanoparticles by using wet chemical method for photocatalytic hydrogen synthesis. Misra et al. [14] synthesized anatase $TiO_2@NiFe_2O_4$ system by using reverse micelle and hydrolysis approach with enhanced photocatalytic activity, but these core@shell nanostructures retained the properties of non-coated $NiFe_2O_4$. Therefore, synthesis of impeccable $MFe_2O_4@TiO_2$ (M = Fe, Sr, Ni, Co, Cu) nanostructures requires more investigation.

The core objective of this research was to synthesize core@shell structured $NiFe_2O_4@TiO_2$ photocatalyst havig enhanced photocatalytic activity for degradation of organic dyes. $NiFe_2O_4@TiO_2$ photocatalyst was synthesis by hydrolysis of a titanium isopropoxide (TTIP) precursor in the presence of $NiFe_2O_4$ nanostructure, whereas $NiFe_2O_4$ NPs were synthesized by sol-gel approach. Characterizations of the $NiFe_2O_4@TiO_2$ photo-catalyst were examined by XRD, SEM, TEM, while BET analysis was carried out for surface area measurement. UV–visible spectroscopy was used to examine the light absorbing activities of the catalyst. VSM was used to investigate magnetic behavior of the nanoparticles. In addition, kinetic study and catalytic activity of photocatalyst were also investigated.

Experimental

Synthesis of the core@shell nanostructure $NiFe_2O_4@TiO_2$ photocatalyst

The core@shell nanostructure was synthesized by sol-gel approach shown in Fig. S1 (supporting information). In (a) step 1, to prepare core material $NiFe_2O_4$, iron nitrate [Fe $(NO_3)_3•5H_2O$], (Sigma-Aldrich) and nickel nitrate [Ni $(NO_3)_2•6H_2O$], (Sigma-Aldrich) were used as the Fe and Ni precursors, respectively, and distilled water as a solvent. Aqueous solutions of iron nitrate and nickel nitrate were prepared by adding 0.2 mol of iron nitrate and 0.1 mol of nickel nitrate in a solvent. The molar ratio of salts M^{3+}/M^{2+} was kept at 2:1. Aqueous solutions of salts were mixed at room temperature and stirred until the mixture was homogenized. The aqueous solution of a chelating agent was prepared by adding 0.15 mol of citric acid and mixed with the nitrate solution. The mixture is then stirred for 1 h followed by neutralization with aqueous ammonia to ensure the hydrolysis of Fe and Ni precursors. The final solution was then evaporated at 80°C until a vigorous gel was formed. The gel was further prone to heat so that the auto combustion starts, and a fluffy like powder was formed. The powder was dried in an oven at 100°C for 2h. The obtained powder was calcined at 600°C for 4 h to produce cubic crystalline $NiFe_2O_4$ nanoparticles. In (b) step 2, the titania was coated on magnetic core $NiFe_2O_4$ as follows: Briefly, 0.15 g of as-synthesized $NiFe_2O_4$ nanoparticles and 0.15 g of cetyl trimethyl ammonium bromide (CTAB) was added into 135 ml (8:1 volume) of n-butanol and anhydrous ethanol solution. The solution is subjected to sonication for 30 min to ensure the complete dispersion of nanoparticles; a few drops of 2 wt. % nitric acid-water solution was added into a mixture. Then 0.12 moles of TTIP in anhydrous ethanol were added dropwise with controlled rhythm in a mixture at room temperature. The weight content of titania was increased in mixture as 10%, 20%, 30% and 40% (w/v %), respectively. The final mixture was further subjected to sonication for 4 h at 75°C. The resulting nanoparticles were then centrifuged and washed with anhydrous ethanol, repeatedly. The precipitates were dried in an oven for 24 h at 100°C. The anatase shell TiO_2 coated $NiFe_2O_4$ was obtained after being calcined at 500°C for 2 h.

Characteristics of the core@shell $NiFe_2O_4@TiO_2$ photocatalyst

Synthesized $NiFe_2O_4$ and $NiFe_2O_4@TiO_2$ nanoparticles were subjected to XRD (STOE-Seifert

X'Pert PRO) using CuKα radiation (λ = 1.5406 °A) at 2θ angles from 20° to 80°. SEM (JEOL-instrument JSM-6490A) executed the morphological study. BET analysis was performed for surface area analysis. The UV-Visible spectra of photocatalyst were obtained by a spectrophotometer (T60 PG Instruments, UK), over the range of 300-900 nm.

Photocatalytic activity

The photocatalytic activity was determined by the photocatalytic degradation of methyl orange dye under a UV lamp. The reaction suspension was prepared by adding 1 mg MO and 0.1 g photocatalyst $NiFe_2O_4@TiO_2$ in 125 ml distilled water. The photocatalytic degradation of methyl orange was performed at ambient temperature. The resulting aqueous solution, comprising the catalyst and the methyl orange, was stirred and placed under UV lamp (300 W Xenon) with cutoff filter 400 nm with the lamp switched off. For the initiation of the photochemical reaction, the lamp was switched on. Samples for analysis (3 ml) were taken after a fixed time interval and centrifuged to separate the photocatalyst. The UV spectrophotometer was used to measure the absorbance of methyl orange dye at given time interval.

Results and Discussion

Structural analysis of NiFe₂O₄and NiFe₂O₄@TiO₂

Fig. 1 shows the indexed XRD patterns of pure $NiFe_2O_4$ and TiO_2 coated $NiFe_2O_4$ nanoparticles prepared using sol-gel auto combustion technique (10%, 20%, 30% and 40% weight content of TiO_2). The broader XRD peaks indicate that the particles have small crystallite sizes and are in nanoscale. It can be observed in Fig. 1 (a) that well phase pure crystalline spinel nickel ferrite has been synthesized with characteristic peaks at 2θ values of 30.278 (d_{220}), 35.645 (d_{311}), 37.309 (d_{222}), 43.346 (d_{400}), 49.463 (d_{331}), 54.043 (d_{422}), 57.408 (d_{511}), and 63.014 (d_{400}) indicating a cubic spinel crystal structure [JCPDS card no 77-0426]. Except for the impure phase of α-Fe_2O_3 (hematite), which is found in all samples. XRD patterns in Fig. 1 (b-e) can be easily indexed as anatase titania comprises of peaks at 2θ values of 25.237 (d_{101}), 37.701 (d_{004}), 48.057 (d_{200}), 54.003 (d_{105}), 55.064 (d_{211}), 62.799 (d_{204}), 70.29 (d_{220}), and 75.127 (d_{215}) [JCPDS card no 04-0477]. $NiFe_2O_4@TiO_2$ did not contain $NiFe_2O_4$ peaks, which shows that the TiO_2 is completely coated with $NiFe_2O_4$ nanoparticles. However, two small peaks at 2θ values of 35.685 (d_{311}), 37.329 (d_{222}) were identified, indicating the presence of $NiFe_2O_4$. The full width at

half maximum (FWHM) values has been used to calculate the crystallite sizes using hkl values and d-spacing. Crystallite sizes were calculated by Debye-Scherrer's equation from the most intense peaks.

$$D = \frac{k\lambda}{\beta Cos\theta}$$

(Where, λ represents wavelength of incident X-rays, k represents shape factor, β represents FWHM in radian while θ represents angle of diffraction). Crystallite sizes were found to be 14 nm ± 2 nm for pure nickel ferrite and 12nm ± 1 nm for titania coated core@shell nanoparticles respectively.

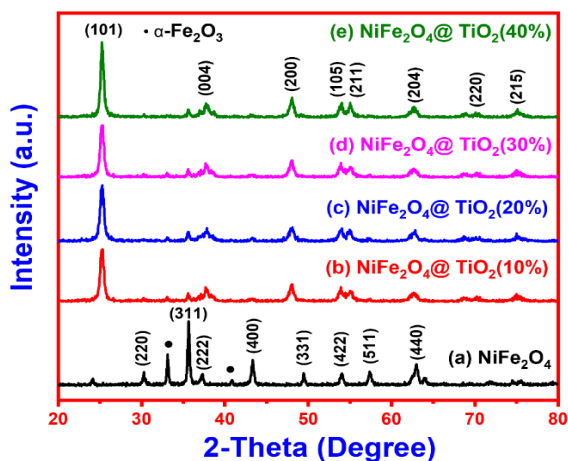Fig 1:   The XRD patterns of $NiFe_2O_4$ and $NiFe_2O_4@TiO_2$ photocatalyst.

Morphological and elemental analysis

Fig. 2 (a-d) shows the SEM images of titania coated nickel ferrite core@shell nanoparticles. SEM determined the morphology and the particle size of the samples at a magnification of 60,000, in which a powder sample was analyzed with dispersion treatment. The morphological analysis revealed that the nano-sized $NiFe_2O_4@TiO_2$ are homogeneous, spherical in shape, uniformly distributed and less agglomerated nanoparticles. Average particle size was found in the range of 16 nm to 24 nm. Elemental composition of the prepared core@shell nanoparticles was found using the inbuilt EDX analysis as shown in Fig. 3 (a) and Table S1 (supporting information). EDX analysis shows composition and mass percentages of constituting elements. It confirms the presence of Ni, Fe, Ti and O atoms. EDX produced atomic ratio for Ti:Fe:Ni in $NiFe_2O_4@TiO_2$ catalyst of 0.17:2.75:1.56. Further, atomic percentages can be verified in elemental X-ray mapping as shown in Fig. 3 (b). The micrographs reveal the homogenous distribution map of the constitute elements of the sample.

Table-1: Surface area, pore volume, pore size and dye degradation efficiency of photocatalyst.

Parameters	Value (w/v %)	
	10% TiO$_2$	40% TiO$_2$
Surface area S$_{BET}$, m^2/g	257.8608	51.896
Pore volume, cm^3/g	2.49956	0.4982
Pore size, A$^\circ$	387.738	469.1847
Degradation efficiency, %	72.69	90.06
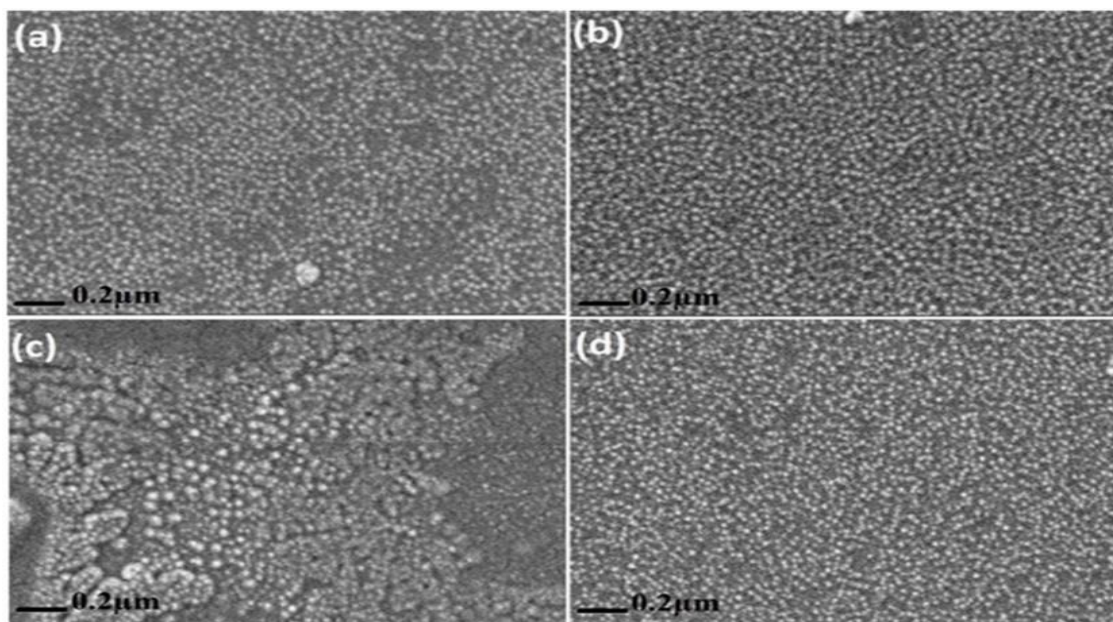
Fig. 2:   SEM photographs of NiFe$_2$O$_4$@TiO$_2$.
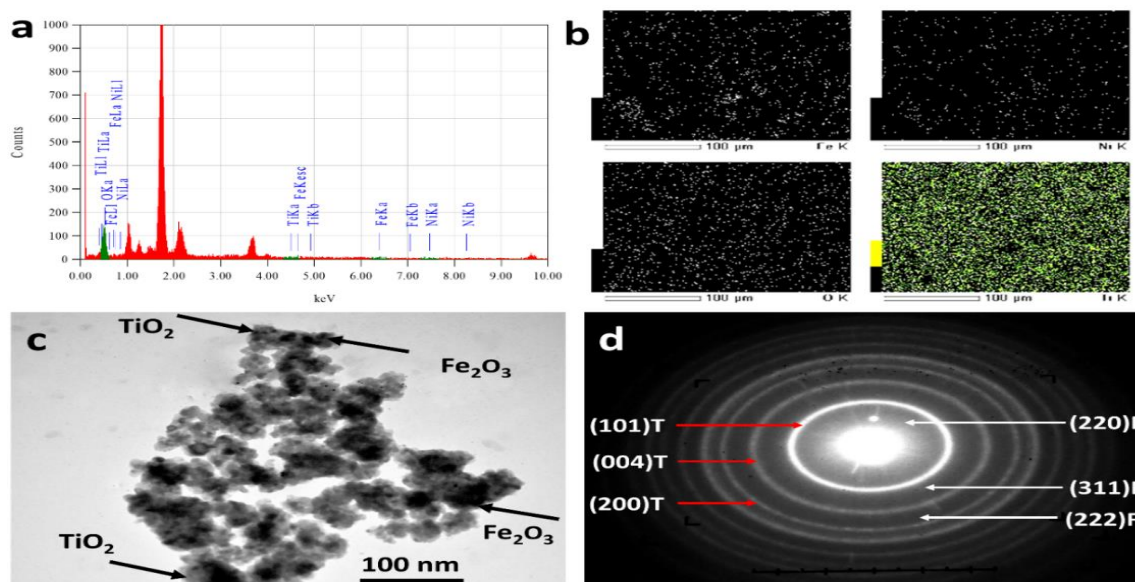
Fig 3:   a) The EDX determined atomic composition of NiFe$_2$O$_4$@TiO$_2$, b) EDX Mapping (Element distribution images), c) TEM photographs of NiFe$_2$O$_4$@TiO$_2$, d) ED pattern of NiFe$_2$O$_4$@TiO$_2$.
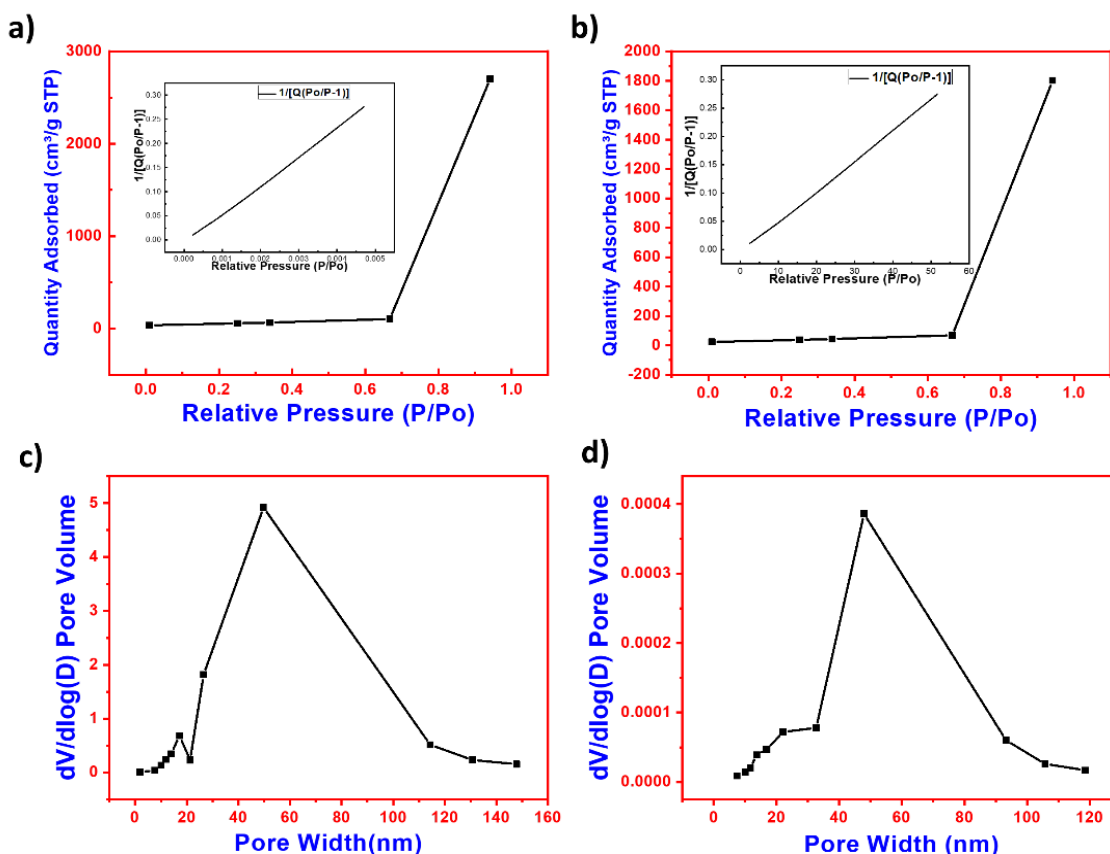
Fig 4:　Nitrogen adsorption-desorption isotherm of the photocatalyst. a) $NiFe_2O_4@TiO_2$ (10%), b) $NiFe_2O_4@TiO_2$ (40%). (c-d) Pore volume and Pore size distribution analysis of both samples respectively.

The morphology of the TiO_2 coated nickel ferrite was further confirmed by TEM. The TEM micrographs are shown in Fig 3 (c). It can clearly observe from the TEM images that the magnetic nickel ferrite is dispersed in TiO_2 coated matrix. The observed particles are rough and irregular in shape. This is to be expected since the ferrite synthesis uses combustion step. The average particle size was found in the range of 14 nm to 20 nm. The typical ED ring pattern of $NiFe_2O_4@TiO_2$ is also shown in Fig 3 (d). The concentric fringes show that the nano-catalyst is polycrystalline in nature.

Surface area analysis

The surface area of NPs is determined by using Brunauer-Emmett-Teller (BET) analysis by nitrogen adsorption-desorption technique. Nitrogen adsorption was executed at 77K in relative pressure range of 0 to 1. N_2 adsorption-desorption isotherm as shown in Fig. 4 (a-b). A low hysteresis value for adsorption and desorption of the coated core@shell

nanostructures can be observed from BET isotherms. The BET surface area of nanoparticles was measured to be 258 m^2/g. The total pore volume of the samples was measured by the nitrogen uptake at $P/P_0 = 0.96$ by using the Barrett-Joyner-Halenda (BJH) method (Fig. 4 (c-d)). The structural parameters including the surface area (S_{BET}), total pore volume (V_{total}), and pore size (D) are shown in Table 1. The larger the surface area, higher will be the active sites, therefore, a high surface area is critically important to enhance the redox reaction sites [33]. The results show that increasing the amount of titania led towards the reduction of surface area. This decrease in surface area was due to thick layer of titania shell on nickel ferrite with an increase in the percent weight content of titanium isopropoxide.

Catalytic activity of $NiFe_2O_4@TiO_2$ core@shell nanostructures

UV-Vis spectroscopy is a powerful mean to examine the light absorbing activities of powder particles. Fig. 5 (a-d) shows the UV-Visible absorption

spectra of MO degradation with $NiFe_2O_4$@TiO_2 in range of 300 nm to 900 nm. The extent of reaction can be measured using the change in absorbance intensity at 460 nm with time. After addition of the core@shell nanoparticles, the reaction has been catalyzed and the peak intensity observed to be decreased with time at 460 nm. This decrease in peak intensity observed to increase while increasing the TiO_2 percent in core@shell nanostructures. Usually, the band gaps of semiconductors are diligently associated with the absorbed wavelength. A smaller band gap of a material will have a larger absorption wavelength. Nickel ferrite nanoparticles correspond to absorption band ranging 200 nm to 710 nm [32]. The result shows that the $NiFe_2O_4$@TiO_2 nanostructures for degradation of MO dye exhibit continuous absorption band. The MO dye with $NiFe_2O_4$@TiO_2 nanostructures presented maximum absorption at 460 nm. The absorption at 460 nm indicates that that the absorption is edge active in a visible region. A band gap (Eg) of $NiFe_2O_4$@TiO_2 nanostructures was calculated from the equation; $E_g=hc/\lambda$
where "h" is a plank constant, "c" is speed of light = 2.988×10^8 ms^{-1}, "λ" is cutoff wavelength at 460 nm corresponding to the band gap of 2.69 eV. The calculated band gap is smaller than pure TiO_2 (3.2 eV). Hence, the presence of $NiFe_2O_4$ nanoparticles improves the absorbance of TiO_2. It's DC resistivity measured by two-probe method observed to decrease with increase in

temperature as shown in the Fig. 7(a). Such behavior can also be helpful as a photocatalytic material because the empty conduction band and completely filled valence band enhances the redox process under a light that could enhance the photocatalytic activity [32].

Photocatalytic degradation and stability

Methyl-orange, belonging to the family of azo dyes is extensively used in textile industry. In order to observe the photo-catalytic activity of core@shell NPs for degradation of MO, UV-Vis spectra were measured at room temperature. The performance of core shell nanoparticles is shown in Fig. 6(a). It can be seen that the concentration of MO dye is inversely related to irradiation time. The decrease in concentration of methyl orange dye from ~25 μmol to ~4 μmol indicates the degradation of the dye. The higher the amount as the TiO_2 in photocatalyst, the more will be the degradation of dye occur. The photostability of the core@shell NPs was determined by performing recycling photoactivity test under UV lamp (300 W Xenon) with cutoff filter 400 nm and is shown in Fig. 6(b) It can be seen that there is no significant loss in the photoactivity of the core@shell NPs photocatalyst during ten successive recycle runs, demonstrating that the excellent photocatalytic efficiency of core@shell NPs.
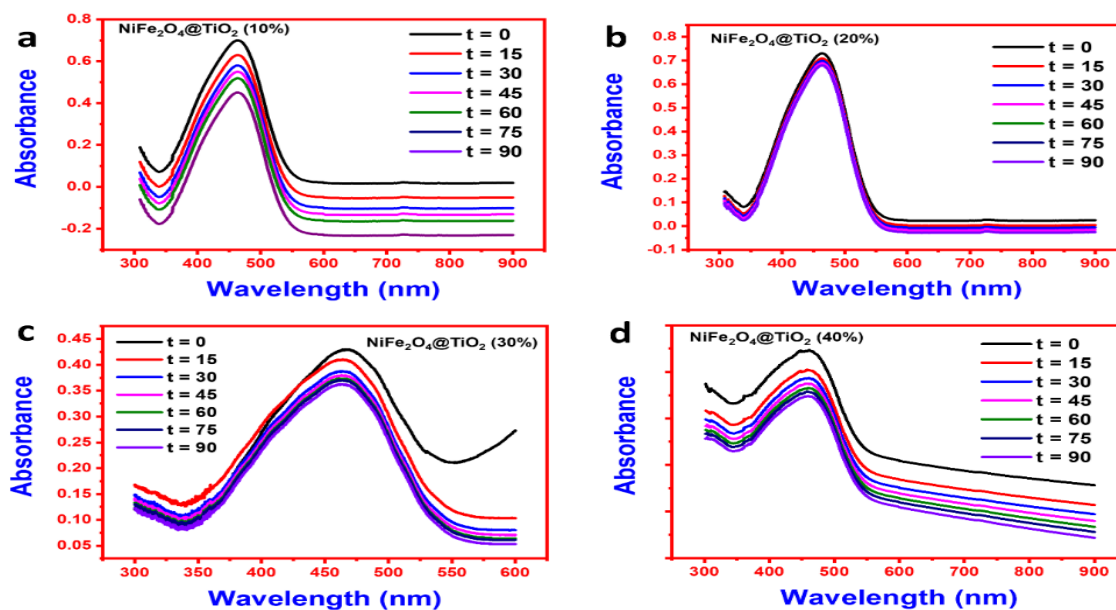

Fig 5:   UV-Visible spectra of a) $NiFe_2O_4$@TiO_2 (10%), b) $NiFe_2O_4$@TiO_2 (20%), c) $NiFe_2O_4$@TiO_2 (30%), d) $NiFe_2O_4$@TiO_2 (40%).

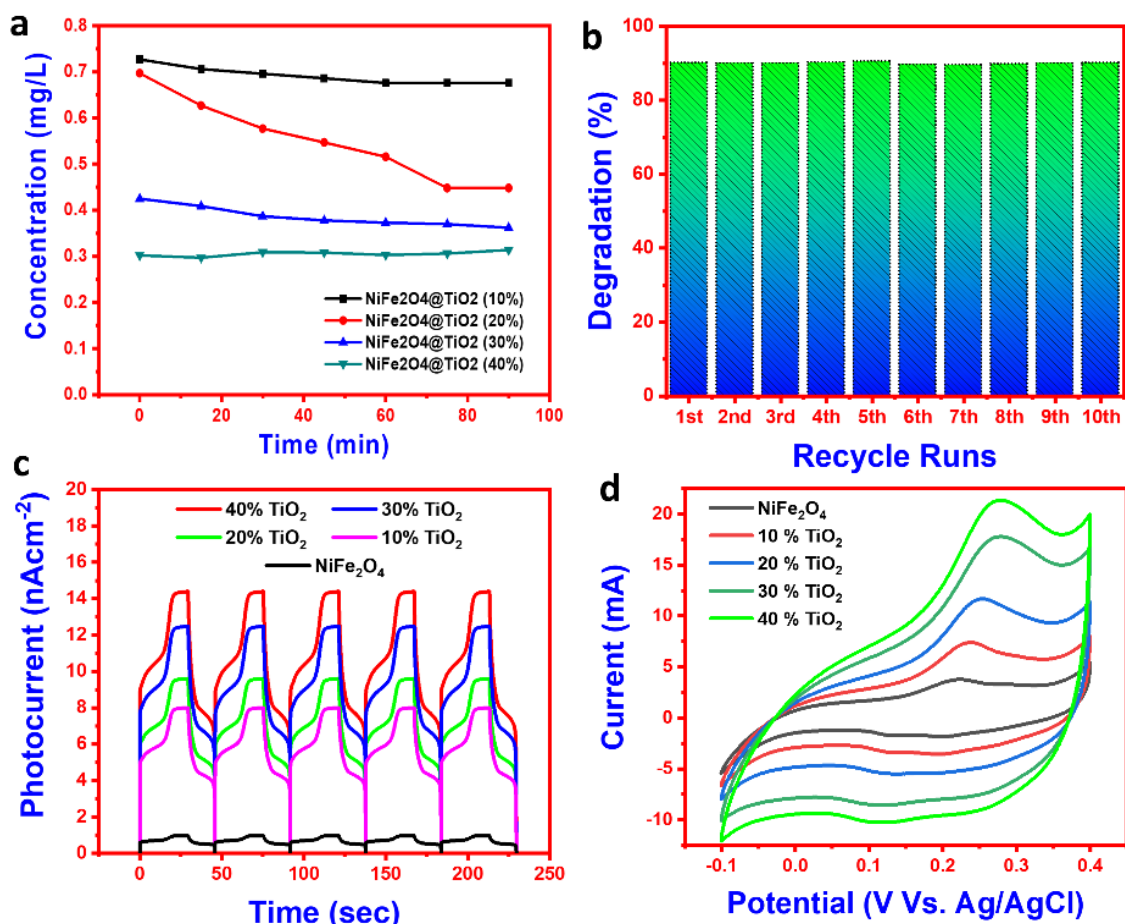Fig 6: a) MO degradation Curve, b) recycling photocatalytic degradation of MO over NiFe$_2$O$_4$@TiO$_2$ (40%) composite, c) transient photocurrent densities profiles of photocatalysts, d) cyclic voltammograms of photocatalysts

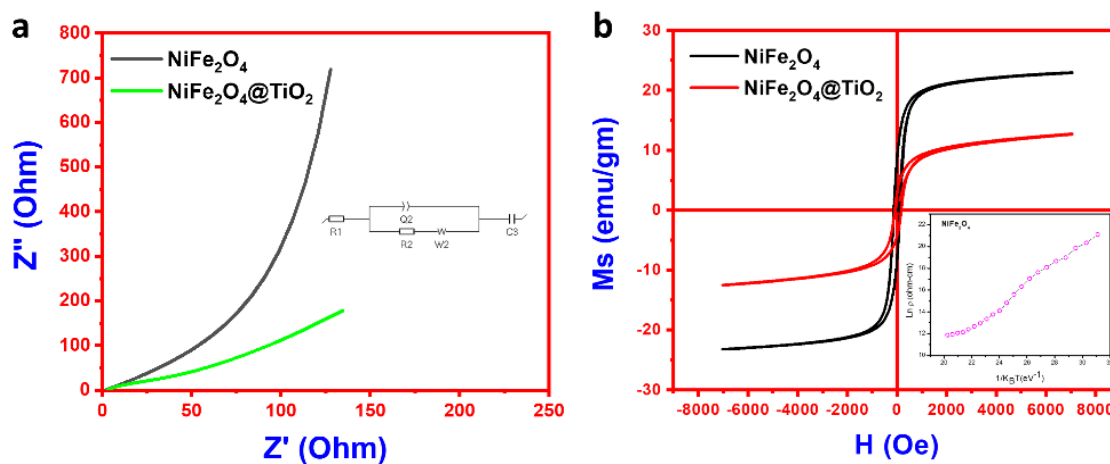Fig 7: a) Impedance analysis (Nyquist plots) for pure NiFe$_2$O$_4$ and NiFe$_2$O$_4$@TiO$_2$ b) M-H curves for pure NiFe$_2$O$_4$ and NiFe$_2$O$_4$@TiO$_2$ (40% TiO$_2$)

Mechanism of the photoactivity improvement

To further investigate the origin of photoactivity enhancement of $NiFe_2O_4@TiO_2$ photocatalyst than $NiFe_2O_4$ and the effect of increasing contents of TiO_2, a photoelectrochemical analysis was performed [36-40]. Fig. 6(c) shows the photocurrent of photocatalysts under periodic on/off of irradiation (400 nm). Bare $NiFe_2O_4$ shows approximately zero photocurrent response when the light is ON, indicating a large bandgap of $NiFe_2O_4$. Whereas as, with coting of TiO_2, the $NiFe_2O_4@TiO_2$ photocatalyst exhibits the photocurrent. As the concentration of TiO_2 is increased, the photocurrent density is also increasing, indicating fast photochemical reactions. Furthermore, the cyclic voltammograms (Fig. 6(d)) of photocatalysts also reveal that with the incensing percentage contents of TiO_2, a significant increase in current density is achieved, which constitute the photocurrent response test. Finally, the electrochemical impedance microscopy was employed to monitor the charge transfer resistance of the photocatalysts on the electrode and at the electrolyte/electrode interface. Fig 7(a) reveals that the $NiFe_2O_4@TiO_2$ has a smaller semicircle diameter than $NiFe_2O_4$, offering less resistance to charge transfer and faster ion diffusion. Hence, the above photoelectrochemical analysis confirmed that the $NiFe_2O_4@TiO_2$ photocatalysts greatly improves efficiency by offering less resistance to photogenerated electrons.

Kinetics of photodegradation reaction of methyl orange

To find out the kinetics (n, k) of degradation reaction, different methods can be utilized, like differential and integral methods of analysis. An integral method of analysis has been chosen to find the kinetic parameters for degradation reaction of MO dye. The relationship between the absorbance (D) and the concentration (C) during the reaction is given by

$$C_0 = \varepsilon(D_\infty - D_0) \qquad (1)$$
$$C = \varepsilon(D_\infty - D) \qquad (2)$$

where C_0 is the concentration at time t = 0, C is the concentration at any time, and ε is molar absorption coefficients at a specified wavelength.

Substituting above equations in Langmuir-Hinshelwood model [34],

$$-\frac{\ln C_{Af}}{C_{A0}} = kt \qquad (3)$$
$$\ln[(D)_\infty - D] = -kt + \ln(D_\infty - D_0) \qquad (4)$$
$$D_\infty - D = (D_\infty - D_0)e^{-kt} \qquad (5)$$

The above equation reveals that the absorbance tends to the value as that of expression in terms of concentration after the completion of a reaction (infinite time). The rate constant can be found by the slope of ln $(D_\infty-D_0)$ vs time graph. The same equation can be expressed in terms of concentration.

Fig. S2 (a-d) (supporting information) shows a plot of ln $(D_\infty - D_0)$ vs time t. All experimental data were well fitted to the first-order kinetics of photo degradation reaction. The result shows the first order kinetic behavior with rate constant k_1 = 0.2021 min^{-1}. The photocatalytic activity was determined by the formula [35].

$$\% \; Photocatalytic \; activity = \frac{C_0 - C}{C_0} \times 100 \qquad (6)$$

The result shows (Table-2) that by increasing the amount of titania the photocatalytic activity of the catalyst is increased.

Table-2: % Photo catalytic activity of as synthesized photocatalyst.

Catalyst	% Photocatalytic Activity
$NiFe_2O_4@TiO_2$ (10%)	72.69
$NiFe_2O_4@TiO_2$ (20%)	80.77
$NiFe_2O_4@TiO_2$ (30%)	88.24
$NiFe_2O_4@TiO_2$ (40%)	90.06

Magnetic analysis

Magnetic behavior and the magnetization of pure nickel ferrite and titania coated nickel ferrites have been measured using M-H loops under the applied magnetic field of 10 kOe at room temperature. Fig. 7(b) shows the required M-H curves of synthesized samples and it can be observed clearly that the magnetization value of pure nickel ferrite has been decreased with a coating of titania shell from 23 emu/g to 14 emu/g. This decrease can be clearly subjected to the presence of non-magnetic material in the powder, as a shell is comprised of TiO_2. This decrease in magnetization is not required for separation of the catalyst, but still a good value of

magnetization can be used for the magnetic separation of the synthesized core@shell nano-catalyst. Ease of catalyst separation and reuse is one of the major issues in heterogeneous catalytic reactions that can be achieved using magnetic core nanomaterials.

Conclusions

The core@shell nanostructures were effectively synthesized by means of sol-gel auto combustion approach. The XRD analysis confirms the synthesis of pure phase nanocrystalline powders. The crystallite sizes were calculated in the range of 12-14 nm±2 nm. The morphological analysis by SEM reveals that the nano-sized $NiFe_2O_4@TiO_2$ are homogeneous, spherical in shape, uniformly distributed and less agglomerated nanoparticles. Average particle size was found in the range of 14.14 nm to 23.57 nm. The Brunauer-Emmett-Teller (BET) analysis was done to measure the surface area of the nanoparticles by nitrogen adsorption-desorption technique. The BET surface area of nanoparticles was measured to be 258 m^2/g. The degradation of methyl orange was photo-catalyzed by as synthesized core@shell nanostructures and its photocatalytic activity was evaluated to be 90.06%. The result shows that the $NiFe_2O_4@TiO_2$ nanostructures for degradation of methyl orange dye exhibit a continuous absorption band. The band gap of $NiFe_2O_4@TiO_2$ nanostructures was determined to be 2.69 eV. The calculated band gap is smaller than pure TiO_2 (3.2 eV). Hence, the presence of $NiFe_2O_4$ nanoparticles improves the absorbance of TiO_2. The integral method of analysis was used to study the kinetic behavior of photochemical reaction. The semi-log plot of dye absorbance versus time is linear, indicating the first order photocatalytic reaction with rate constant k_1 = 0.2021 min^{-1}.

References

1. K. Tanaka, K. Padermpole and T. Hisanaga, Photocatalytic degradation of commercial azo dyes, *Wat. Res.*, **34**, 327 (2000).
2. S. Sakthivel, Neppolian, M. V. Shankar, B. Arabindoo, M. Palanichamy and V. Murugesan, Solar photocatalytic degradation of azo dye: comparison of photocatalytic efficiency of ZnO and TiO_2, Sol. *Energy Mater. Sol. Cells*, **77**, 65 (2003).
3. I. K. Konstantinou and T. A. Albanis, TiO_2-assisted photocatalytic degradation of azo dyes in aqueous solution: kinetic and mechanistic investigations A review, *Appl. Catal. B.*, **49**, 1 (2004).
4. H. M. Xiao, X. M. Liu and S. Y. Fu, Synthesis, magnetic and microwave absorbing properties of core-shell structured $MnFe_2O_4/TiO_2$ nanocomposites, Compos. *Struct. Tech.*, **66**, 2003 (2006).
5. D. Spasiano, R. Marotta, S. Malato, P. Fernandez-Ibañez and I. Di Somma, Solar photocatalysis: Materials, reactors, some commercial, and pre-industrialized applications. A comprehensive approach, *Appl. Catal. B.*, **48**, 170 (2015).
6. T. Zhang, X. Wang and X. Zhang, Recent Progress in TiO_2-Mediated Solar Photocatalysis for Industrial Wastewater Treatment, *Int. J. Photoenergy,* **22,** 12, (2014).
7. H. Nguyen and S. A. El-Safty, Meso- and Macroporous Co_3O_4 Nanorods for Effective VOC Gas Sensors, *J. Phy. Chem. C.*, **115**, 8466 (2011).
8. R. Benrabaa, H. Boukhlouf, A. Löfberg, A. Rubbens, R. N. Vannier and E. Bordes-Richard, Nickel ferrite spinel as catalyst precursor in the dry reforming of methane: Synthesis, characterization and catalytic properties, *J. Nat. Gas Chem.*, **21**, 595 (2012).
9. Q. Zhang, J. J. Wang, C. F. Lin, Y. H. Jing and C. T. Chang, Photoreduction of carbon dioxide by graphene–titania and zeolite–titania composites under low-intensity irradiation, *Mat. Sci. Semi. Proc.*, **30**, 162 (2015).
10. A. M. Ferrari Lima, R. P. de Souza, S. S. Mendes, R. G. Marques, M. L. Gimenes and N. R. C. Fernandes Machado, Photodegradation of benzene, toluene and xylenes under visible light applying N-doped mixed TiO_2 and ZnO catalysts, *Catal. Today*, **241**, 40 (2015).
11. Y. N. Chang, X. M. Ou, G. M. Zeng, J. L. Gong, C. H. Deng and Y. Jiang, Synthesis of magnetic graphene oxide TiO_2 and their antibacterial properties under solar irradiation, *Appl. Surf. Sci.*, **343**, 10 (2015).
12. Q. I. Rahman, M. Ahmad, S. K. Misra and M. B. Lohani, Hexagonal ZnO nanorods assembled flowers for photocatalytic dye degradation: Growth, structural and optical properties, *Superlattices Microstr.*, **64**, 495, (2013).
13. P. Sathishkumar, R. V. Mangalaraja, S. Anandan and M. Ashokkumar, $CoFe_2O_4/TiO_2$ nanocatalysts for the photocatalytic degradation of Reactive Red 120 in aqueous solutions in the presence and absence of electron acceptors, *Chem. Eng. J.*, **220**, 302 (2013).
14. S. Rana, R. S. Srivastava, M. M. Sorensson and R. D. K. Misra, Synthesis and characterization of

nanoparticles with magnetic core and photocatalytic shell: Anatase TiO_2–$NiFe_2O_4$ system, *Mat. Sci. Eng. B.*, **119**, 144 (2005).

15. C. L. Bianchi, C. Pirola, F. Galli, G. Cerrato, S. Morandi and V. Capucci, Pigmentary TiO_2: A challenge for its use as photocatalyst in NOx air purification, *Chem. Eng. J.*, **261**, 76 (2015).

16. I. D. Somma, L. Clarizia, S. Satyro, D. Spasiano, R. Marotta and R. Andreozzi, A kinetic study of the simultaneous removal of EDDS and cupric ions from acidic aqueous solutions by TiO_2-based photocatalysis under artificial solar light irradiation and deaerated batch conditions, *Chem. Eng. J.*, **270**, 519 (2015).

17. H. Dzinun, M. H. D. Othman, A. F. Ismail, M. H. Puteh, M. A. Rahman and J. Jaafar, Photocatalytic degradation of nonylphenol by immobilized TiO_2 in dual layer hollow fibre membranes, *Chem. Eng. J.*, **269**, 255 (2015).

18. H. Huang, H. Huang, L. Zhang, P. Hu, X. Ye and D. Y. C. Leung, Enhanced degradation of gaseous benzene under vacuum ultraviolet (VUV) irradiation over TiO_2 modified by transition metals, *Chem. Eng. J.*, **259**, 534 (2015).

19. A. R. Khataee and M. B. Kasiri, Photocatalytic degradation of organic dyes in the presence of nanostructured titanium dioxide: Influence of the chemical structure of dyes, *J. Mol. Catal. A: Chem.*, **328**, 8 (2010).

20. C. K. Ngaw, Q. Xu, T. T. Y. Tan, P. Hu, S. Cao and J. S. C. Loo, A strategy for in-situ synthesis of well-defined core–shell Au@TiO_2 hollow spheres for enhanced photocatalytic hydrogen evolution, *Chem. Eng. J.*, **257**, 112 (2014).

21. V. Vaiano, O. Sacco, D. Sannino and P. Ciambelli, Photocatalytic removal of spiramycin from wastewater under visible light with N-doped TiO_2 photocatalysts, *Chem. Eng. J.*, **261**, 3 (2015).

22. S. M. Zacarías, M. L. Satuf, M. C. Vaccari and O. M. Alfano, Photocatalytic inactivation of bacterial spores using TiO_2 films with silver deposits, *Chem. Eng. J.*, **266**, 133 (2015).

23. R. Tejasvi, M. Sharma and K. Upadhyay, Passive photo-catalytic destruction of air-borne VOCs in high traffic areas using TiO_2-coated flexible PVC sheet, *Chem. Eng. J.,* **262**, 875 (2015).

24. X. Tang, B. Y. Zhao, Q. Tian and K. A. Hu, Synthesis, characterization and microwave absorption properties of titania-coated barium ferrite composites, *J. Phy. Chem. Solids*, **67**, 2442 (2006).

25. S. Mohammadi, A. Harvey and K. V. K. Boodhoo, Synthesis of TiO_2 nanoparticles in a spinning disc reactor, *Chem. Eng. J.*, **258**, 171 (2014).

26. J. Huo, Y. Hu, H. Jiang, X. Hou and C. Li, Continuous flame synthesis of near surface nitrogen doped TiO_2 for dye-sensitized solar cells, *Chem. Eng. J.*, **258**, 163 (2014).

27. T. K. Houlding, P. Gao, V. Degirmenci, K. Tchabanenko and E. V. Rebrov, Mechanochemical synthesis of TiO_2/$NiFe_2O_4$ magnetic catalysts for operation under RF field, *Mat. Sci. Eng. B.*, **193**, 175 (2015).

28. D. He, Y. Sun, L. Xin and J. Feng, Corrigendum to Aqueous tetracycline degradation by non-thermal plasma combined with nano-TiO_2, *Chem. Eng.* J., **262**, 18 (2015).

29. J. Feng, J. Zhu, W. Lv, J. Li and W. Yan, Effect of hydroxyl group of carboxylic acids on the adsorption of Acid Red G and Methylene Blue on TiO_2, *Chem. Eng. J.*, **269**, 316 (2015).

30. S. Chowdhury, G. K. Parshetti and R. Balasubramanian, Post-combustion CO_2 capture using mesoporous TiO_2/graphene oxide nanocomposites, *Chem. Eng. J.*, **263**, 374 (2015).

31. M. Baudys, J. Krýsa, M. Zlámal and A. Mills, Weathering tests of photocatalytic facade paints containing ZnO and TiO_2, *Chem. Eng. J.*, **261**, 83 (2015).

32. H. S. Kim, D. Kim, B. S. Kwak, G. B. Han, M.-H. Um and M. Kang, Synthesis of magnetically separable core@shell structured $NiFe_2O_4$@TiO_2 nanomaterial and its use for photocatalytic hydrogen production by methanol/water splitting, *Chem. Eng. J.*, **243**, 272 (2014).

33. K. Kočí, L. Obalová, L. Matějová, D. Plachá, Z. Lacný and J. Jirkovský., Effect of TiO_2 particle size on the photocatalytic reduction of CO_2, *Appl. Catal. B: Envir.*, **89**, 494 (2009).

34. K. V. Kumar, K. Porkodi and F. Rocha, Langmuir–Hinshelwood kinetics – A theoretical study, *Catal. Commun.*, **9**, 82 (2008).

35. F. A. Harraz, R. M. Mohamed, M. M. Rashad, Y. C. Wang and W. Sigmund, Magnetic nanocomposite based on titania–silica/cobalt ferrite for photocatalytic degradation of methylene blue dye, *Ceram. Int.*, **40**, 375 (2014).

36. Z. Chen and Y. Xu, Ultrathin TiO2 Layer Coated-CdS Spheres Core−Shell Nanocomposite with Enhanced Visible-Light Photoactivity, ACS *Appl. Mater. Interfaces.*, **5**, 13353 (2013).

37. N. Zhang, S. Liu, X. Fu and Y. Xu, Fabrication of coenocytic Pd@CdS nanocomposite as a visible light photocatalyst for selective transformation under mild conditions, *J. Mater. Chem.,* **22**, 5042 (2012).

38. N. Zhang, S. Liu and Y. Xu, Recent progress on metal core@semiconductor shell nanocomposites as a promising type of photocatalyst, *Nanoscale*, **4**, 2227 (2012).

39. B. Weng, K. Q. Lu, Z. Tang, H. M. Chen, Y. Xu, Stabilizing ultrasmall Au clusters for enhanced photoredox catalysis, *Nat. Commun.*, **9**, 1543, (2018).

40. S. Liu, N. Zhang, and Y. Xu, Core–Shell Structured Nanocomposites for Photocatalytic Selective Organic Transformations, Part. Part. *Syst. Charact.*, **31**, 540 (2014).